Dehydrogenase E1 and transketolase domain-containing protein 1 – DHTKD1

A Target Enabling Package (TEP)

Gene ID / UniProt ID / EC	55526 / Q96HY7 / 1.2.4.2EC
Target Nominator	Stefan Kölker (University Hospital Heidelberg)
Authors	Gustavo A. Bezerra[1], William R. Foster[1], Henry J. Bailey[1], Kevin G. Hicks[2], Sven W. Sauer[3], Bianca Dimitrov[3], Thomas J. McCorvie[1], Jurgen G. Okum[3], Jared Rutter[2], Stefan Kölker[3], Wyatt W. Yue[1]
Target PI	Dr Wyatt Yue (Oxford)
Therapeutic Area(s)	Rare, metabolic diseases
Disease Relevance	DHTKD1 is gene upstream of GCDH, the molecular cause of Glutaric aciduria type I (OMIM 231670)
Date Approved by TEP Evaluation Group	November 27th 2020
Document version	2.0
Document version date	January 2021
Citation	Gustavo A. Bezerra, William R. Foster, Henry J. Bailey, Kevin G. Hicks, Sven W. Sauer, Bianca Dimitrov, … Wyatt W. Yue. (2020). Dehydrogenase E1 and transketolase domain-containing protein 1 (DHTKD1); A Target Enabling Package [Data set]. Zenodo. http://doi.org/10.5281/zenodo.4428229
Affiliations	[1]Centre for Medicines Discovery, Nuffield Department of Medicine, University of Oxford. [2]Department of Biochemistry, University of Utah School of Medicine, USA.[3]Division of Child Neurology and Metabolic Medicine, Centre for Pediatrics and Adolescent Medicine, Clinic I, University Hospital Heidelberg, Germany.

USEFUL LINKS

(Please note that the inclusion of links to external sites should not be taken as an endorsement of that site by the SGC in any way)

SUMMARY OF PROJECT

Inherited mutations of the *GCDH* gene for glutaryl-CoA dehydrogenase, catalysing the sixth enzymatic step in lysine catabolism, lead to the rare neurometabolic disorder Glutaric Aciduria type 1 (GA1). There is a rationale that inhibition of the fifth lysine catabolising step, catalysed by the DHTKD1 enzyme, could provide therapeutic benefit for GA1 by means of substrate reduction. This TEP provides early tools to develop DHTKD1 inhibitors, including recombinant protein, structure, biophysical (activity and stability) assays and fragment hits of human DHTKD1. This work also reports the interaction of DHTKD1 with its functional partner DLST as a binary complex, and an EM reconstruction of the DLST catalytic core.

SCIENTIFIC BACKGROUND

Pathway of lysine degradation

In mammals, the catabolism of lysine takes place via nine enzymatic steps, beginning with lysine oxidation to 2-aminoadipate semialdehyde, which is converted to 2-oxoadipate and further broken down to glutaryl-CoA, and then to acetyl-CoA, for entry into the TCA cycle (**Fig 1**). The DHTKD1 enzyme (Dehydrogenase E1 and transketolase domain-containing protein 1) catalyses the fifth step, namely the oxidative decarboxylation of 2-oxoadipate (OA) into their glutaryl-CoA, generating NADH.
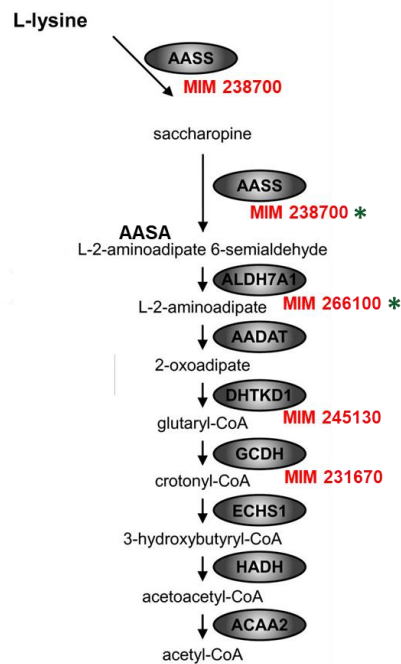

Figure 1. Summary of the lysine catabolic pathway. The first two steps are catalysed by a single bifunctional protein (AASS). OMIM IDs for associated genetic diseases in the pathway are shown. Asterisks indicate structure (ALDH7A1) & TEP (AASS) previously reported by the group.

DHTKD1 belongs to the family of 2-oxoacid dehydrogenases which catalyse the oxidative decarboxylation of 2-oxoacids (e.g. pyruvate, 2-oxoisovalerate, 2-oxoglutarate, 2-oxoadipate) into their corresponding acyl-CoA thioester, generating the reducing equivalent NADH. The overall reaction is dissected into three sequential steps each catalysed by an individual enzyme (1). In the first and rate-limiting step, the E1 enzyme (a 2-oxoacid decarboxylase) catalyses the irreversible decarboxylation of 2-oxoacids via the thiamine diphosphate (ThDP) cofactor and subsequent transfer of the decarboxylated acyl intermediate on an oxidised dihydrolipoyl prosthetic group that is covalently amidated to the E2 enzyme (a dihydrolipoyl acyltransferase). In the second step, E2 transfers the acyl moiety from the dihydrolipoyl group onto a co-enzyme A acceptor, generating acyl-CoA and a reduced dihydrolipoyl group. In the final step, one FAD-dependent E3 enzyme (dihydrolipoamide dehydrogenase, DLD) universal to all E1 and E2, re-oxidises the dihydrolipoyl group by transferring one reducing equivalent of NAD$^+$ to yield NADH.

Multiple copies of the E1, E2 and E3 components assemble into a supramolecular complex reaching 4-10 MDa (2). The 2-oxoadipate dehydrogenase complex (OADHc) is composed of DHTKD1 as the E1, dihydrolipoamide succinyltransferase (DLST) as E2, and the universal (DLD) as E3. Recently, Zhang et al (3) have shown that the correct assembly of DHTKD1 and DLST is necessary for the proper functioning of OADHc, using variants that disrupted the DHTKD1-DLST interaction. Furthermore, the contact interface for DHTKD1-DLST was mapped using hydrogen-deuterium exchange mass spectrometry (HDX-MS) and chemical cross-linking coupled with mass spectrometry (XL-MS).

Disease linkage

Glutaric aciduria type I (GA1, OMIM 231670) is a rare but severe cerebral organic aciduria of lysine degradation, caused by the autosomal recessive inherited deficiency of glutaryl-CoA dehydrogenase (GCDH). GCDH is a mitochondrial enzyme catalysing the sixth step of lysine catabolism (Fig 1). GCDH deficiency leads to accumulation of lysine degradation intermediates, such as neurotoxic glutaric acid (GA), 3-hydroxyglutaric acid (3-OHGA) and glutaryl-CoA. The estimated overall prevalence is 1 in 100 000 newborns (4). There is no universally adopted therapy beyond diet restriction and anti-convulsants.

Therapeutic rationale

DHTKD1 acts upstream of GCDH (Fig 1), and its deficiency leads to none or often mild clinical phenotypes in humans, such as 2-aminoadipic 2-oxoadipic aciduria (OMIM **204750**). Therefore, it has been proposed that inhibiting human DHTKD1 (hDHTKD1) to reduce the accumulation of GCDH substrates and derivatives is a viable therapeutic intervention to decrease glutaryl-CoA levels (5). This approach of 'substrate reduction', to mitigate the toxic accumulation of a metabolite that arises from a metabolic block by inhibiting an enzyme upstream of it, has found successful application in other inborn errors of metabolism(6), and have been the subject of four other TEP projects from this programme(7) (8) (9) (10).

The overall objective of this TEP is to provide discovery tools of hDHTKD1 (crystal structure, biophysical assays, fragment hits) for exploration of the therapeutic concept.

RESULTS – THE TEP

Proteins Purified

We obtained soluble expression in *E. coli* for the mitochondrial precursor protein $hDHTKD1_{1–919}$, the predicted mature protein ($hDHTKD1_{23–919}$), and a truncated construct ($hDHTKD1_{45–919}$) removing the putatively disordered aa 24–44 (**Fig 2A**). We also reconstructed seven hDHTKD1 missense variants (**Fig 2A**) that are associated with 2-aminoadipic and 2-oxoadipic aciduria, including p.L234G, p.Q305H, p.R455Q, p.R715C, p.G729R, p.P773L and p.S777P. With the exception of p.L234G and p.S777p, the variant proteins are solubly expressed in *E. coli* like the wild-type (WT).
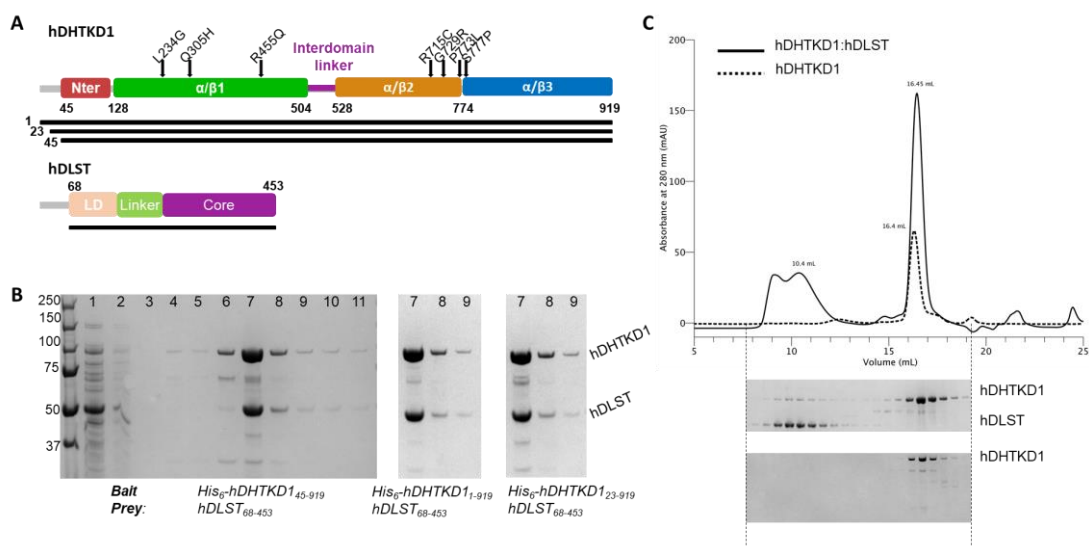

Figure 2. Proteins expressed and purified during this work. **(A)** Domain organisation of hDHTKD1 and hDLST constructs. 7 diseases variants are indicated by arrows on hDHTKD1 schematic. **(B)** SDS-PAGE showing affinity pulldown of untagged $hDLST_{68-453}$ from His_6-tagged $hDHTKD1_{45-919}$. Lanes include: 1, flow-through; 2-6, wash fractions of increasing imidazole concentration; 7-11, elution fractions with 250 mM imidazole. **(C)** Chromatogram and SDS-PAGE from size exclusion chromatography runs of $hDHTKD1_{45-919}$ protein alone (dashed line), and of $hDHTKD1_{45-919}$ co-expressed with $hDLST_{68-453}$ in *E. coli*. Elution volumes for the complex peak and hDHTKD1-alone peak are shown.

For interaction studies, we have co-expressed the DHTKD1-DLST binary complex in *E. coli*, by co-transformation of a plasmid that encodes His-tagged hDHTKD1 and a plasmid encoding untagged hDLST. We confirmed using this system that hDHTKD1$_{45-919}$ and hDLST$_{68-453}$ can form a direct interaction (**Fig 2B,C**). Additionally, the DHTKD1-DLST complex was also generated by co-infection of hDHTKD1$_{45-919}$-expressing baculovirus and DLST$_{68-453}$-expressing baculovirus in insect Sf9 cells. The complex is further purified by size exclusion chromatography using an analytical Superose 6 Increase column.

In vitro Assays

Enzyme activity
We measured hDHTKD1 activity by following the reduction of 2,6-dichlorophenolindophenol (DCPIP), which acts as an artificial electron acceptor for the E1 reaction, at $\lambda = 610$-750 nm. We confirmed that hDHTKD1$_{45-919}$ displays E1 decarboxylase activity with 2-oxoadipate (2OA) as substrate, presenting a $V_{max} = 14.2$ µmol min^{-1}mg^{-1} protein, and $K_{M, 2OA} = 0.2$ mM.

Metabolite interactome
In collaboration with the Rutter group (University of Utah), we mapped the metabolite interactome of hDHTKD1 using a mass spectrometry-based equilibrium dialysis approach ('MIDAS')(11). From screening a library of 412 human metabolites, we observed that 2OA presented the most significant interaction with hDHTKD1 in the presence of ThDP and Mg^{2+} (**Fig 3A**). In this assay, we also confirmed that hDHTKD1 is able to process 2OA, indicated by the most negative Log2(corrected fold change) value (-1.17) observed for this compound.

Thermostability of DHTKD1 variants
We characterised the five hDHTKD1 variants that are solubly expressed using differential scanning fluorimetry (DSF) to compare their thermostability with WT protein. Among them, only p.P773L exhibited a significantly reduced change in the melting temperature ($\Delta T_m = -5.2$°C) (**Fig 3B**), suggesting that this mutation alters thermostability of the protein.

Protein-protein pull-down
Our DHTKD1-DLST co-expression system in *E. coli* allows untagged hDLST to be co-purified with His-tagged hDHTKD1 immobilised on Ni affinity resin. We have used this pull-down assay to evaluate the importance of hDHTKD1 N-terminal region for interaction with hDLST. We found that untagged hDLST$_{68-453}$ was pulled down in a similar manner by His-tagged hDHTKD1$_{1-919}$, hDHTKD1$_{23-919}$ and hDHTKD1$_{45-919}$ (**Fig 2B**). This suggests that the hDHTKD1 N-terminal 45 aa, which differs from the equivalent region in hOGDH, does not play a role in the DHTKD1–DLST interaction.

Impact of DHTKD1 variants on interaction with DLST
We next performed similar pull-down assay using the above hDHTKD1 missense variants, and observed that the hDHTKD1 p.R715C variant showed an impaired ability to interact with hDLST$_{68-453}$ (**Fig 3C**), suggesting that the hDHTKD1 p.R715C mutation disrupts complex formation with hDLST.
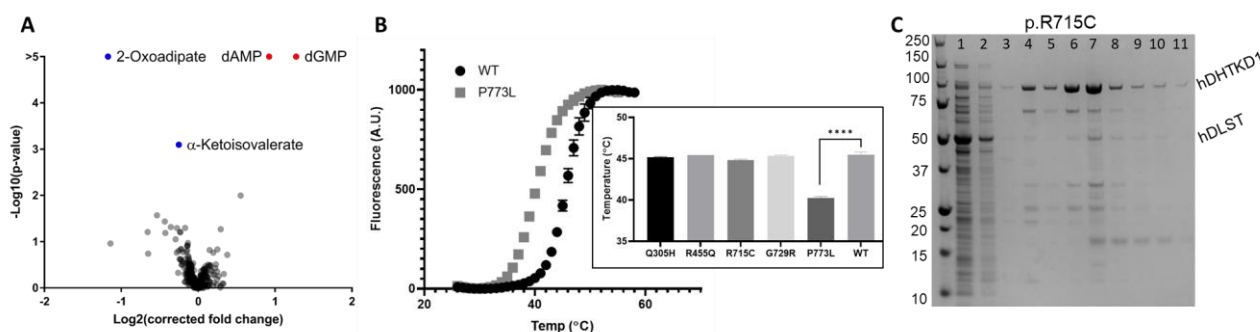

Figure 3. Biophysical characterisation of hDHTKD1. (**A**) The hDHTKD1-metabolite interactome as determined by MIDAS. hDHTKD1 significantly depleted 2OA and a related metabolite α-oxoisovalerate (blue dots) and enriched two deoxypurine monophosphate ligands namely dAMP and dGMP (red dots). The cut-off for significance was $p < 0.05$, q <

0.1. **(B)** DSF melting curves for hDHTKD1$_{45-919}$ wt and p.P773L, with inset showing the derived melting temperature (T$_M$) values for wt and 5 variants. **(C)** Affinity pulldown of hDLST$_{68-453}$ by immobilised His-tagged hDHTKD1$_{45-919}$ p.R715C variant.

Structural data

DHTKD1 Overall fold

Amongst different hDHTKD1 constructs, we succeeded in crystallising hDHTKD1$_{45-919}$ pre-incubated with the cofactor ThDP and Mg^{2+} ion, and determined its structure to 1.9 Å resolution. Two DHTKD1 molecules are present in the asymmetric unit (**Fig 4A**), arranged as an intertwined obligate homodimer in a similar manner to the structurally characterised homologue of *E. coli* 2-oxoglutarate dehydrogenase (OGDH). hDHTKD1$_{45-919}$ crystal homodimer is consistent with SAXS analysis in solution, with the theoretical scattering curve of the dimer displaying a good fit to experimental data (χ2 of 3.8, **Fig 4B**).

The DHTKD1 protomer consists of an N-terminal helical bundle (aa 53-127) followed by three α/β domains (α/β1: aa 129-496, Pfam PF00676; α/β2: aa 528-788, PF02779; α/β3: aa 789-915, PF16870). These four structural regions assemble into two halves, inter-connected by an extended linker (aa 497-527) that threads along the protein surface (**Fig 4C**).

Mapping the seven reported DHTKD1 missense mutations onto the structure, three (p.L234G, p.Q305H, p.R455Q) are located within the α/β1 domain, while the other four (p.R715C, p.G729R, p.P773L, p.S777P) are clustered in the α/β2 domain (**Fig 4C**). The destabilising p.P773L mutation (**Fig 3B**) affects Pro773 that crucially forms a bend at a surface exposed loop. Its substitution to Leu likely alters the structural integrity of this loop.
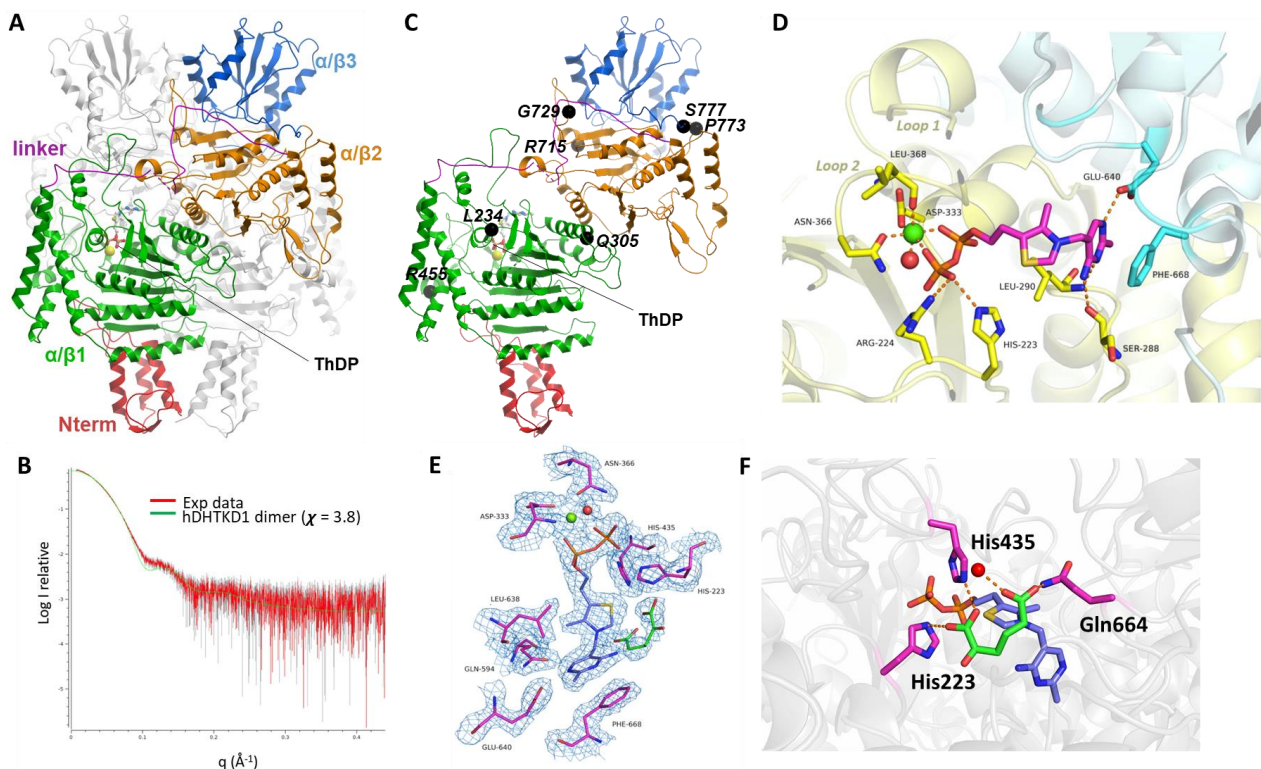

Figure 4. hDHTKD1 overall structure. **(A)** Homodimer crystal structure of hDHTKD1, one subunit is coloured according to Fig 2A and the other is represented in grey. **(B)** SAXS theoretical scattering profile of hDHTKD1$_{45-919}$ homodimer (green line) is compared to the experimental scattering profile (red lines). **(C)** Structural locations of missense mutations, depicted as black spheres, on one hDHTKD1 protomer. **(D)** ThDP co-factor (magenta sticks) binding site. Residues forming this site originate from both subunits (shown as yellow and blue sticks). Hydrogen bonds are shown as orange dashed lines. **(E)** Simulated annealing 2Fo-Fc composite map of DHTKD1 active site contoured at 1 σ, depicting the co-factor ThDP (blue lines) and 2OA (green lines). Mg^{2+} is represented as a green sphere and a water molecule is represented as

a red sphere. **(F)** Binding environment of the modelled 2OA ligand; same colour scheme as panel E. This figure was prepared using hDHTKD1 coordinates determined in this work (PDB code 6SY1).

Active site

Each DHTKD1 subunit in the crystal homodimer is bound with a ThDP cofactor, at a site formed from both subunits and highly conserved among OGDH and E1 homologues (**Fig 4D**). For instance, residues Asp333 and Asn336 form a bridge between ThDP pyrophosphates and the Mg^{2+} ions, while Leu290 acts as a hydrophobic wedge forming the typical V-shaped conformation of ThDP. Surprisingly, in one crystallographic dataset, we observed OMIT map electron density at one active site of the homodimer which does not correspond to the co-factor or any component present in the crystallization condition (**Fig 4E**). This density is located in the vicinity of the ThDP co-factor, although it is not directly connected to it. The size of this density feature can accommodate a C6 ligand such as 2OA without covalent linkage to ThDP. Although the observed ligand, likely co-purified with the protein, did not undergo enzymatic turnover, the keto carbon can be placed at 3.5 Å from the ThDP thiazolium C2 and hence be compatible with the nucleophilic attack and subsequent decarboxylation (**Fig 4F**). While in good agreement with OMIT map, the 2OA model was not included in the deposited structure, in light of no further experimental evidence of its presence.

Cryo-EM reconstruction of DLST catalytic core

We performed single-particle cryo-EM on the binary complex of hDHTKD1$_{45-919}$-hDLST$_{68-453}$ co-expressed in *Sf9 cells*, to understand a structural context for the interactions. Electron micrographs revealed the characteristic cubic cage structures, with approximate dimensions of 130 Å x 130 Å x 130 Å (**Fig 5A and Fig 5B**), which are similar to that which has been described in the literature for *E. coli* DLST (12). Full-length hDLST comprises (**Figs. 2A, 5C**) the N-terminal lipoyl attachment domain (LD) connected by a flexible linker to the C-terminal catalytic and multimerisation core. Our EM reconstruction allows the assignment of 24 hDLST C-terminal cores assembled as eight trimer building blocks into a cubic cage with octahedral symmetry (**Fig 5C**). The first visible residue (aa 219) of all C-terminal cores are surface-exposed (**Fig 5C, inset**), presumably projecting the hDLST N-terminal domain to engage the E1 (DHTKD1) and E3 (DLD) components of OADHc. Unfortunately, there is no visible EM density that could account for the DLST N-terminal domain or DHTKD1 present in our binary complex. We hypothesise that DLST lipoyl domain and adjoining linker are highly flexible, and the interaction between DHTKD1 and DLST are transient.
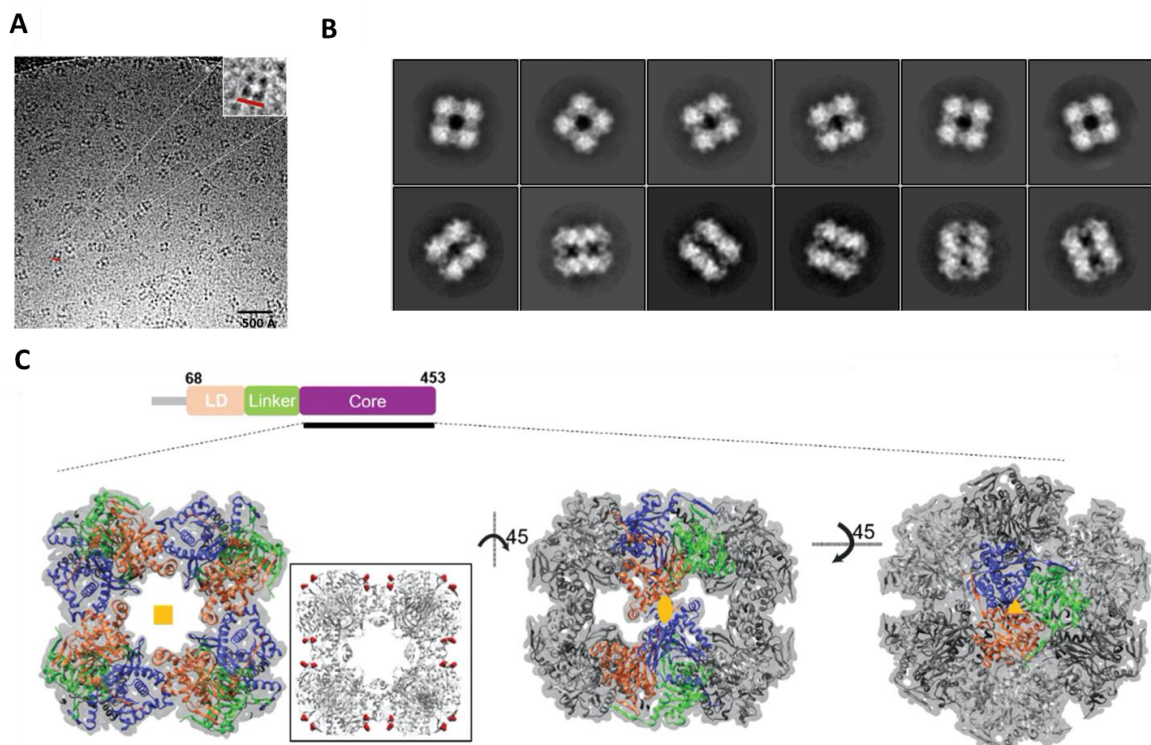
Figure 5. Characterisation of hDHTKD1-hDLST complex by cryo-EM. **(A)** Electron micrograph of Sf9-co-expressed hDHTKD1$_{45-919}$-hDLST$_{68-453}$ sample. **(B)** 12 2D classes of the sample showed in panel A. **(C)** EM Map of the hDLST 24-mer catalytic core, overlaid with a humanized model of *E. coli* DLST (PDB 1SCZ). The three views show how the trimer building block (monomers shown as blue, orange and green ribbons) are assembled into the 24-mer core via four-fold (left), two-fold (middle) and three-fold (right) symmetry axes respectively. Inset of the left view shows how the first residue (aa 219, red spheres) from each of the 24 hDLST catalytic cores are distributed at the surface of the cube structure.

Chemical Matter

To identify chemical matter as starting points for hDHTKD1 inhibitor design, we carried out a crystallography-based fragment screening campaign (XChem). Diffraction data sets from 178 hDHTKD1 crystals, each soaked with an individual fragment, have been collected and processed. The campaign yielded 6 crystals displaying 12 binding events across 6 pockets, which are described below (**Fig 6**). The two active sites of the hDHTKD1 homodimer are deeply buried, accessed only by two narrow channels and, as expected, no fragment was observed binding at the active site. Nevertheless, the six fragment binding sites are found in functionally relevant regions for two properties of the hDHTKD1 enzyme.

Fragments in proximity to mapped DLST-interacting regions
Five of the fragment binding sites are close to previously mapped DLST-interacting residues from HDX-MS and XL-MS studies (3) (**Fig 6**). We propose that these fragments can be developed into inhibitors with the potential of disrupting the interaction between hDHTKD1 and hDLST, and hence function of the OADHc complex.

Binding site 2
Fragment **b** is accommodated, via its quinoxaline group, between residues Leu530 and Phe533 from helix α23 (aa 527-538), Ala584 from helix α26 (aa 570-585) and, via its OH containing aromatic group, loop Met623-Phe630 (**Fig 7A**). OD1 and OD2 from Asp624 make polar contacts with O01 and N09 from the fragment, respectively. Two previously reported DHTKD1-DLST cross-links are located close to this fragment. hDHTKD1 Lys628, which is at a distance of approximately 6 Å from fragment **b**, cross-links with lysines 85 and 159 of hDLST. hDHTKD1 Lys537, which is 7.2 Å apart from fragment **b**, cross-links with lysines 98, 219, 289 and 373 of hDLST.
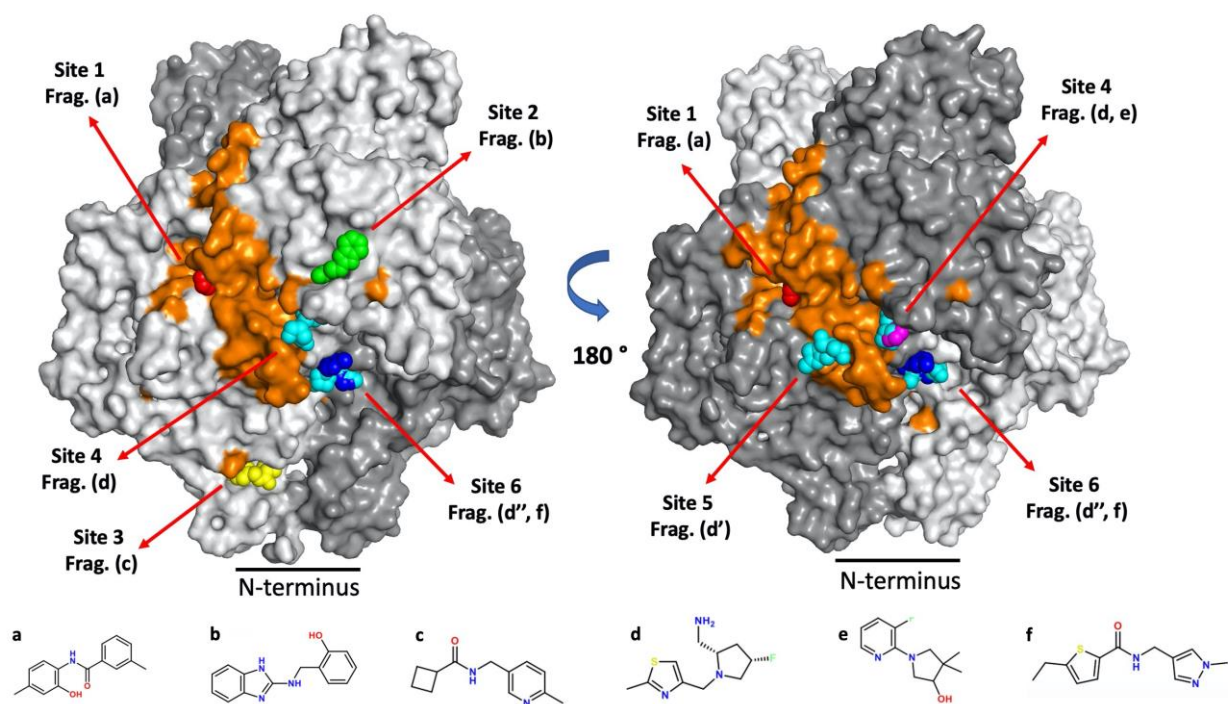
Figure 6. Fragments bound to hDHTKD1 are distributed across 6 different sites. Surface representation of hDHTKD1, where each subunit is coloured in different shades of grey. Fragments **a-f** chemical structures are shown at the bottom of the figure. hDHTKD1 surface areas mapped to interact with DLST in previous studies are shown in orange.

Binding site 3
Fragment **c** is located at the N-terminal region of DHTKD1, accommodated between helices α1 (aa 53-67), α4 (aa114-127), α5 (aa139-156) and loop Phe100-Glu111 (**Fig 7B**). 4 lysines present in this region were identified by XL-MS experiments to interact with DHTKD1. For example, fragment **c** is at a distance of approximately 7.5 Å from Lys143, which cross-links with lysines 87 and 98 of DLST. Fragment **c** is also at a distance of approximately 6.8 Å from Lys148, which cross-links with lysines 24, 66, 78, 150, 159, 286, 289, 342 and 373 of DLST.

Binding site 4
Fragments **d** and **e** are accommodated in the pocket formed by Phe630 and Glu632 from strand β16 (aa 630-636), and are facing residues Trp313-Pro315, which are part of an 'aa 291-328' region mapped by HDX-MS to interact with hDLST (**Fig 7C**). Moreover, hDHTKD1 Lys628 is at a distance of approximately 9 Å from fragments **d** and **e** and cross-links with lysines 85 and 159 of DLST. Note that fragment **d** is also observed to bind in two other positions (**d'** and **d''**) as described below.

Binding site 5
Fragment **d'** is located in the vicinity of fragments and **d** and **e,** separated by the loop Asp310-Arg324 and helix α11 (aa 292-309) (**Fig 7C**). Fragment **d'** is accommodated in a pocket formed by Gln309, Pro315, Asp316 and Arg324, which are part of the DLST-interacting region aa 291-328 from HDX-MS.

Binding site 1
For hDHTKD1 crystal soaked with fragment **a**, we observed ligand difference density in a pocket accommodated between the loop Leu503-Trp509 and strands β3 (aa 268-271) and β4 (aa 279-284), facing residues Ser268 and His280 (**Fig 7D**). The binding pocket is also formed by residues Lys300, Arg304 and Arg308 from helix α11 (aa 292-309). The loop Leu503-Trp509 is part of a hDLST-interacting region 'aa485-518' mapped by HDX-MS. Additionally, the binding pocket residue Lys300 was identified by XL-MS to interact with hDLST. In this data set, the loop Leu503-Trp509 is displaced from the unliganded conformation (**Fig 7D**), likely a consequence of fragment binding. Unfortunately, accurate placement of the fragment was not possible because its electron density is not sufficiently defined, therefore this crystal structure was not deposited.

Fragments close to DHTKD1 homodimer interface
hDHTKD1 is an obligate homodimer, with its active site being formed by residues originating from both subunits. We envisage that fragments found at the hDHTKD1 dimer interface have the potential for further inhibitor development aimed at disrupting hDHTKD1 dimerisation and hence its enzymatic activity.

Binding site 6
Fragments **d''** and **f** are located at hDHTKD1 dimerisation region, accommodated in a groove formed by residues Ala374-Ser380 of one subunit and facing residues Asn350-Pro353 of the opposite subunit (**Fig 7E**). Both fragments are present in the equivalent regions (symmetrically related) of hDHTKD1 chain A and B. O1 and N1 from fragment **f** make polar contacts with main chain oxygen of Ser379 and Glu375, respectively.

Assays to validate chemical matters
We propose employing the affinity pull-down assay described in page 4, where an untagged hDLST is co-purified with His-tagged hDHTDK1 immobilised on Ni affinity resin, to verify whether chemical matters further developed from this TEP project will be able to disrupt or impair complex formation. Furthermore, the impact on DHTKD1-DLST complex formation can also be characterised via size exclusion chromatography using an analytical Superose 6 Increase column.
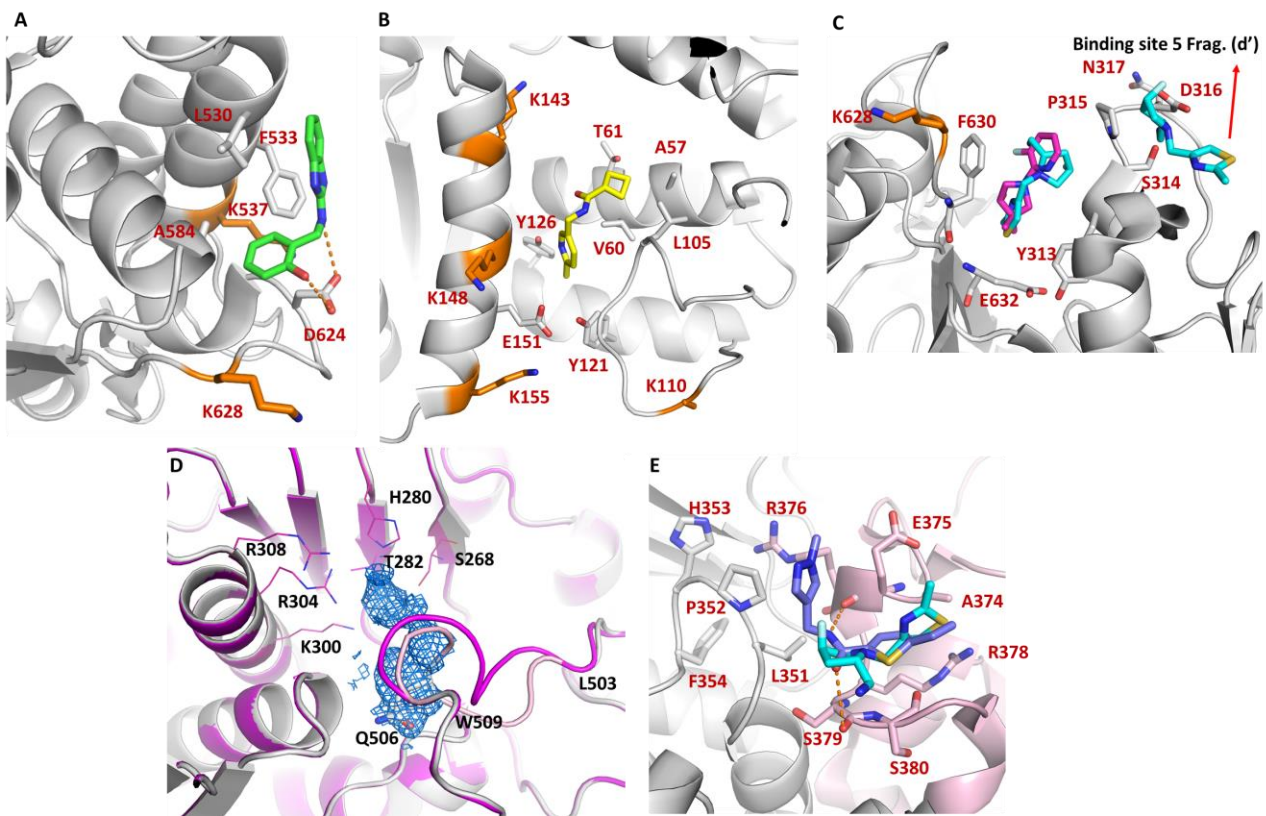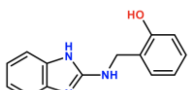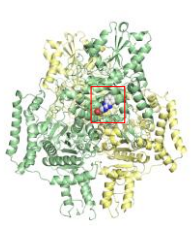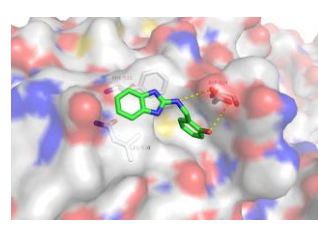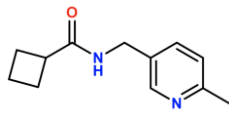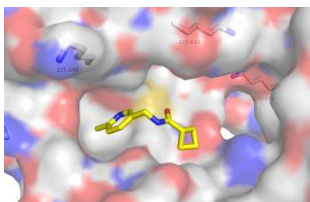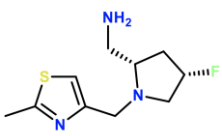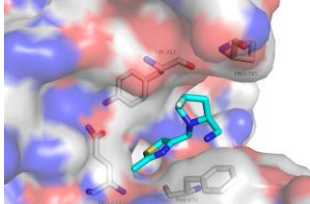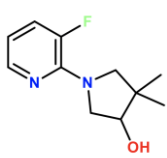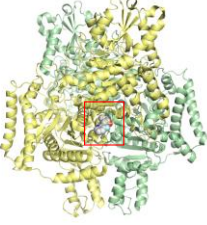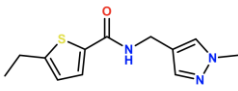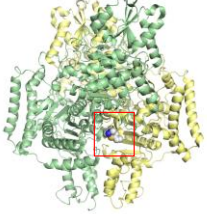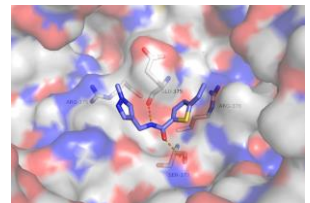
Figure 7. Binding sites of DHTKD1 bound to fragments. **(A) Binding site 2**, residues forming fragment **b** (shown as green sticks) binding pocket are shown as grey sticks. DHTKD1 Lys537 and Lys628, which cross-links with DLST are depicted as orange sticks. **(B) Binding site 3**, residues forming fragment **c** (yellow) binding pocket are shown as grey sticks. DHTKD1 lysines which cross-link with DLST are shown as orange sticks. **(C) Binding sites 4 and 5**, residues forming the binding pocket of fragment **d** (shown as cyan sticks) and fragment **e** (shown as magenta sticks) and are depicted as grey sticks. **Binding site 5**, residues forming fragment **d'** binding pocket, which is opposed to **Binding site 4**, are shown as grey sticks. **(D)** Difference density was observed in **Binding site 1**, when hDHTKD1 crystal was soaked with fragment **a**. Residues forming this pocket are shown as sticks. DHTKD1 ground-state model is shown in dark grey. Gln506 conformation in the ground-state model is shown as grey sticks. PanDDA event map contoured at 1σ is shown as a blue mesh. **(E) Binding site 6**, residues forming the binding pocket of fragment **d''** (shown as cyan sticks) and fragment **f** (shown as blue sticks) are shown as sticks. One DHTKD1 subunit is coloured in pink and the opposite subunit is coloured in grey. Polar contacts are indicated as orange dashed lines.
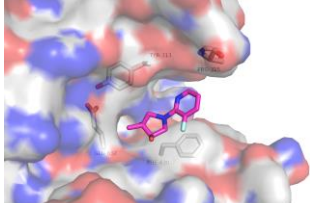
PDB ID	Ligand	Binding location	Binding pocket	Resolution (Å)
[5RVW](#) fragment **b**	Z1587220559			1.61 Å

[5RVY](#) fragment **c**	 Z437516460			1.60 Å
[5RW0](#) fragment **d**	 Z2444997446			1.67 Å
[5RVZ](#) fragment **e**	 Z1929757385			1.98 Å
[5RVX](#) fragment **f**	 Z804566442			1.66 Å

IMPORTANT: Please note that the existence of small molecules within this TEP indicates only that chemical matter might bind to the protein in potentially functionally relevant locations. The small molecule ligands are intended to be used as the basis for future chemistry optimisation to increase potency and selectivity and yield a chemical probe or lead series. As such, the molecules within this TEP should not be used as tools for functional studies of the protein, unless otherwise stated, as they are not sufficiently potent or well-characterised to be used in cellular studies.

Other components

Commercially available CRISPR/Cas9 knockout plasmids
SCBT: **Cat # sc-407613**
Genscript: **55526**
These sgRNA sequences were validated in Sanjana N.E., Shalem O., Zhang F. Improved vectors and genome-wide libraries for CRISPR screening. Nat Methods. 2014, 11(8):783-4.
Commercially available antibodies
Thermofisher: **Product # PA5-65197**
SCBT: **sc-398620 (monoclonal)**

CONCLUSION

This TEP presents the first crystal structure of DHTKD1, a component of the 2-oxoadipate dehydrogenase complex (OADHc). DHTKD1 plays an important role in lysine and tryptophan degradation, which is considered clinically relevant because its malfunctioning can result in two severe inborn errors of metabolism: Pyridoxine-dependent epilepsy and Glutaric aciduria type I. The latter is caused by glutaryl-CoA dehydrogenase (GCDH) deficiency, resulting in accumulation of toxic metabolites. DHTKD1 is located immediately upstream of GCDH and its inhibition has been proposed as a therapeutic intervention to treat this condition, by substrate reduction approach.

The correct assembly of DHTKD1 and the DLST component of OADHc has been shown to be important for the formation of glutaryl-CoA. Our data provides insight into how DHTKD1 and DLST interact with each other in a multi-subunit fashion that culminates in the assembly of a megadalton complex. We also provide chemical fragments that bind to DHTKD1, with potential for small molecule drug discovery by preventing the DHTKD-DLST interaction and therefore impairing OADHc activity. Future compounds can be validated for their impact, using the DHTKD1-DLST interaction and pulldown assays presented in this work. As future work, we will aim to develop an OADHc activity assay reported from the literature, which measures the overall reactions of E1, E2 and E3 components leading to glutaryl-CoA formation (3)(13). To this end, we have already generated the E3 component protein (dihydrolipoamide dehydrogenase, DLD) from recombinant expression.

Additionally, DHTKD1 is an emerging player as a contributor of reactive oxygen species (ROS) development in mitochondria and we envisage that the chemical matters provided in this work can be developed for probing the role of DHTKD1 in mitochondrial function, particularly those related to energy production and ROS balance.

TEP IMPACT

Publications arising from this work:
Parts of this work have been recently published: Bezerra et al., *Crystal structure and interaction studies of human DHTKD1 provide insight into a mitochondrial megacomplex in lysine catabolism*. IUCrJ, 2020. **7**, 693-706.

FUNDING INFORMATION

ADDITIONAL INFORMATION

Structure Files

PDB ID	Structure details	Resolution (Å)
6SY1	Structure of DHTKD1 bound with TPP	1.87
5RW1	Structure of DHTKD1 ground-state model	1.52
5RVW	Structure of DHTKD1 bound with TPP and fragment **b** (x0048): 2-[(1H-benzimidazol-2-ylamino)methyl]phenol	1.61
5RVY	Structure of DHTKD1 bound with TPP and fragment **c** (x0164): N-[(6-methylpyridin-3-yl)methyl]cyclobutanecarboxamide	1.60
5RW0	Structure of DHTKD1 bound with TPP and fragment **d** (x0173) ((2S,4S)-4-fluoro-1-((2-methylthiazol-4-yl)methyl)pyrrolidin-2-yl)methanamine	1.67
5RVZ	Structure of DHTKD1 bound with TPP and fragment **e** (x0166): 1-(3-fluoropyridin-2-yl)-4,4-dimethylpyrrolidin-3-ol	1.98
5RVX	Structure of DHTKD1 bound with TPP and fragment **f** (x0095): 5-ethyl-N-[(1-methylpyrazol-4-yl)methyl]thiophene-2-carboxamide	1.66
EMDB ID		
EMD-11014	Cryo-EM map of human dihydrolipoamide succinyltransferase catalytic domain (DLST)	4.70

Materials and Methods

Protein Expression and Purification

hDHTKD1$_{45-919}$ for crystallisation
SGC ID: DHTKD1A-c002
Vector: pNIC28-Bsa4
Accession: Q96HY7, NM_018706.6
Cell line: *E. coli Rosetta*
Tags and additions: N-terminal, TEV protease cleavable hexa-histidine tag.
Construct Protein Sequence:

MHHHHHHSSGVDLGTENLYFQ*SMGALERPPVDHGLARLVTVYCEHGHKAAKINPLFTGQALLENVPEIQALVQTLQGPF
HTAGLLNMGKEEASLEEVLVYLNQIYCGQISIETSQLQSQDEKDWFAKRFEELQKETFTTEERKHLSKLMLESQEFDHFLATKF
STVKRYGGEGAESMMGFFHELLKMSAYSGITDVIIGMPHRGRLNLLTGLLQFPPELMFRKMRGLSEFPENFSATGDVLSHLT
SSVDLYFGAHHPLHVTMLPNPSHLEAVNPVAVGKTRGRQQSRQDGDYSPDNSAQPGDRVICLQVHGDASFCGQGIVPETF
TLSNLPHFRIGGSVHLIVNNQLGYTTPAERGRSSLYCSDIGKLVGCAIIHVNGDSPEEVVRATRLAFEYQRQFRKDVIIDLLCYR
QWGHNELDEPFYTNPIMYKIIRARKSIPDTYAEHLIAGGLMTQEEVSEIKSSYYAKLNDHLNNMAHYRPPALNLQAHWQGL
AQPEAQITTWSTGVPLDLLRFVGMKSVEVPRELQMHSHLLKTHVQSRMEKMMDGIKLDWATAEALALGSLLAQGFNVRLS
GQDVGRGTFSQRHAIVVCQETDDTYIPLNHMDPNQKGFLEVSNSPLSEEAVLGFEYGMSIESPKLLPLWEAQFGDFFNGAQI
IFDTFISGGEAKWLLQSGIVILLPHGYDGAGPDHSSCRIERFLQMCDSAEEGVDGDTVNMFVVHPTTPAQYFHLLRRQMVR
NFRKPLIVASPKMLLRLPAAVSTLQEMAPGTTFNPVIGDSSVDPKKVKTLVFCSGKHFYSLVKQRESLGAKKHDFAIIRVEELCP
FPLDSLQQEMSKYKHVKDHIWSQEEPQNMGPWSFVSPRFEKQLACKLRLVGRPPLPVPAVGIGTVHLHQHEDILAKTFA
(underlined sequence contains vector encoded His-tag and TEV protease cleavage site*)

hDHTKD1$_{1-919}$
SGC ID: DHTKD1A-c014
Vector: pCDF-LIC
Accession: Q96HY7, NM_018706.6
Cell line: *E. coli Rosetta*
Tags and additions: N-terminal, TEV protease cleavable hexa-histidine tag.
Construct Protein Sequence:

MHHHHHHSSGVDLGTENLYFQ*SMASATAAAARRGLGRALPLLWRGYQTERGVYGYRPRKPESREPQGALERPPVDHGL
ARLVTVYCEHGHKAAKINPLFTGQALLENVPEIQALVQTLQGPFHTAGLLNMGKEEASLEEVLVYLNQIYCGQISIETSQLQSQ
DEKDWFAKRFEELQKETFTTEERKHLSKLMLESQEFDHFLATKFSTVKRYGGEGAESMMGFFHELLKMSAYSGITDVIIGMP
HRGRLNLLTGLLQFPPELMFRKMRGLSEFPENFSATGDVLSHLTSSVDLYFGAHHPLHVTMLPNPSHLEAVNPVAVGKTRGR
QQSRQDGDYSPDNSAQPGDRVICLQVHGDASFCGQGIVPETFTLSNLPHFRIGGSVHLIVNNQLGYTTPAERGRSSLYCSDIG
KLVGCAIIHVNGDSPEEVVRATRLAFEYQRQFRKDVIIDLLCYRQWGHNELDEPFYTNPIMYKIIRARKSIPDTYAEHLIAGGLM
TQEEVSEIKSSYYAKLNDHLNNMAHYRPPALNLQAHWQGLAQPEAQITTWSTGVPLDLLRFVGMKSVEVPRELQMHSHLL
KTHVQSRMEKMMDGIKLDWATAEALALGSLLAQGFNVRLSGQDVGRGTFSQRHAIVVCQETDDTYIPLNHMDPNQKGFL
EVSNSPLSEEAVLGFEYGMSIESPKLLPLWEAQFGDFFNGAQIIFDTFISGGEAKWLLQSGIVILLPHGYDGAGPDHSSCRIERF
LQMCDSAEEGVDGDTVNMFVVHPTTPAQYFHLLRRQMVRNFRKPLIVASPKMLLRLPAAVSTLQEMAPGTTFNPVIGDSS
VDPKKVKTLVFCSGKHFYSLVKQRESLGAKKHDFAIIRVEELCPFPLDSLQQEMSKYKHVKDHIWSQEEPQNMGPWSFVSPR
FEKQLACKLRLVGRPPLPVPAVGIGTVHLHQHEDILAKTFA

(underlined sequence contains vector encoded His-tag and TEV protease cleavage site*)

hDHTKD1₍₂₅₋₉₁₉₎

SGC ID: DHTKD1A-c015
Vector: pCDF-LIC
Accession: Q96HY7, NM_018706.6
Cell line: *E. coli Rosetta*
Tags and additions: N-terminal, TEV protease cleavable hexa-histidine tag.
Construct Protein Sequence:
MHHHHHHSSGVDLGTENLYFQ*SMGYQTERGVYGYRPRKPESREPQGALERPPVDHGLARLVTVYCEHGHKAAKINPLFT
GQALLENVPEIQALVQTLQGPFHTAGLLNMGKEEASLEEVLVYLNQIYCGQISIETSQLQSQDEKDWFAKRFEELQKETFTTEE
RKHLSKLMLESQEFDHFLATKFSTVKRYGGEGAESMMGFFHELLKMSAYSGITDVIIGMPHRGRLNLLTGLLQFPPELMFRK
MRGLSEFPENFSATGDVLSHLTSSVDLYFGAHHPLHVTMLPNPSHLEAVNPVAVGKTRGRQQSRQDGDYSPDNSAQPGDR
VICLQVHGDASFCGQGIVPETFTLSNLPHFRIGGSVHLIVNNQLGYTTPAERGRSSLYCSDIGKLVGCAIIHVNGDSPEEVVRAT
RLAFEYQRQFRKDVIIDLLCYRQWGHNELDEPFYTNPIMYKIIRARKSIPDTYAEHLIAGGLMTQEEVSEIKSSYYAKLNDHLNN
MAHYRPPALNLQAHWQGLAQPEAQITTWSTGVPLDLLRFVGMKSVEVPRELQMHSHLLKTHVQSRMEKMMDGIKLDW
ATAEALALGSLLAQGFNVRLSGQDVGRGTFSQRHAIVVCQETDDTYIPLNHMDPNQKGFLEVSNSPLSEEAVLGFEYGMSIE
SPKLLPLWEAQFGDFFNGAQIIFDTFISGGEAKWLLQSGIVILLPHGYDGAGPDHSSCRIERFLQMCDSAEEGVDGDTVNMF
VVHPTTPAQYFHLLRRQMVRNFRKPLIVASPKMLLRLPAAVSTLQEMAPGTTFNPVIGDSSVDPKKVKTLVFCSGKHFYSLVK
QRESLGAKKHDFAIIRVEELCPFPLDSLQQEMSKYKHVKDHIWSQEEPQNMGPWSFVSPRFEKQLACKLRLVGRPPLPVPAV
GIGTVHLHQHEDILAKTFA

(underlined sequence contains vector encoded His-tag and TEV protease cleavage site*)

hDHTKD1₍₄₅₋₉₁₉₎ for co-expression in E. coli

SGC ID: DHTKD1A-c016
Vector: pCDF-LIC
Accession: Q96HY7, NM_018706.6
Cell line: *E. coli Rosetta*
Tags and additions: N-terminal, TEV protease cleavable hexa-histidine tag.
Construct Protein Sequence:
MHHHHHHSSGVDLGTENLYFQ*SMGALERPPVDHGLARLVTVYCEHGHKAAKINPLFTGQALLENVPEIQALVQTLQGPF
HTAGLLNMGKEEASLEEVLVYLNQIYCGQISIETSQLQSQDEKDWFAKRFEELQKETFTTEERKHLSKLMLESQEFDHFLATKF
STVKRYGGEGAESMMGFFHELLKMSAYSGITDVIIGMPHRGRLNLLTGLLQFPPELMFRKMRGLSEFPENFSATGDVLSHLT
SSVDLYFGAHHPLHVTMLPNPSHLEAVNPVAVGKTRGRQQSRQDGDYSPDNSAQPGDRVICLQVHGDASFCGQGIVPETF
TLSNLPHFRIGGSVHLIVNNQLGYTTPAERGRSSLYCSDIGKLVGCAIIHVNGDSPEEVVRATRLAFEYQRQFRKDVIIDLLCYR
QWGHNELDEPFYTNPIMYKIIRARKSIPDTYAEHLIAGGLMTQEEVSEIKSSYYAKLNDHLNNMAHYRPPALNLQAHWQGL
AQPEAQITTWSTGVPLDLLRFVGMKSVEVPRELQMHSHLLKTHVQSRMEKMMDGIKLDWATAEALALGSLLAQGFNVRLS
GQDVGRGTFSQRHAIVVCQETDDTYIPLNHMDPNQKGFLEVSNSPLSEEAVLGFEYGMSIESPKLLPLWEAQFGDFFNGAQI
IFDTFISGGEAKWLLQSGIVILLPHGYDGAGPDHSSCRIERFLQMCDSAEEGVDGDTVNMFVVHPTTPAQYFHLLRRQMVR
NFRKPLIVASPKMLLRLPAAVSTLQEMAPGTTFNPVIGDSSVDPKKVKTLVFCSGKHFYSLVKQRESLGAKKHDFAIIRVEELCP
FPLDSLQQEMSKYKHVKDHIWSQEEPQNMGPWSFVSPRFEKQLACKLRLVGRPPLPVPAVGIGTVHLHQHEDILAKTFA

(underlined sequence contains vector encoded His-tag and TEV protease cleavage site*)

hDLST₆₈₋₄₅₃ for co-expression in E. coli

hDLST$_{68-453}$ for co-expression in E. coli

SGC ID: DLSTA-c019
Vector: pNIC-CT10HStII
Accession: P36957, NM_001933.4
Cell line: *E. coli Rosetta*
Tags and additions: C-terminal His$_{10}$ tag and Tandem Strep TagII tag, preceded by a TEV protease cleavage site.
Construct Protein Sequence:
MDDLVTVKTPAFAESVTEGDVRWEKAVGDTVAEDEVVCEIETDKTSVQVPSPANGVIEALLVPDGGKVEGGTPLFTLRKTGA
APAKAKPAEAPAAAAPKAEPTAAAVPPPAAPIPTQMPPVPSPSQPPSGKPVSAVKPTVAPPLAEPGAGKGLRSEHREKMNR
MRQRIAQRLKEAQNTCAMLTTFNEIDMSNIQEMRARHKEAFLKKHNLKLGFMSAFVKASAFALQEQPVVNAVIDDTTKEV
VYRDYIDISVAVATPRGLVVPVIRNVEAMNFADIERTITELGEKARKNELAIEDMDGGTFTISNGGVFGSLFGTPIINPPQSAIL
GMHGIFDRPVAIGGKVEVRPMMYVALTYDHRLIDGREAVTFLRKIKAAVEDPRVLLLDL

hDHTKD1₄₅₋₉₁₉ for co-infection in Sf9

hDHTKD1$_{45-919}$ for co-infection in Sf9

SGC ID: DHTKD1A-c012
Vector: pFB-Bio5
Accession: Q96HY7, NM_018706.6
Cell line: Sf9
Tags and additions: His$_6$ tag in 22-aa N-terminal fusion peptide, with TEV protease cleavage site and C-terminal biotin attachment site.
Construct Protein Sequence:
MGHHHHHHSSGVDLGTENLYFQ*SMGALERPPVDHGLARLVTVYCEHGHKAAKINPLFTGQALLENVPEIQALVQTLQGP
FHTAGLLNMGKEEASLEEVLVYLNQIYCGQISIETSQLQSQDEKDWFAKRFEELQKETFTTEERKHLSKLMLESQEFDHFLATK
FSTVKRYGGEGAESMMGFFHELLKMSAYSGITDVIIGMPHRGRLNLLTGLLQFPPELMFRKMRGLSEFPENFSATGDVLSHL
TSSVDLYFGAHHPLHVTMLPNPSHLEAVNPVAVGKTRGRQQSRQDGDYSPDNSAQPGDRVICLQVHGDASFCGQGIVPET
FTLSNLPHFRIGGSVHLIVNNQLGYTTPAERGRSSLYCSDIGKLVGCAIIHVNGDSPEEVVRATRLAFEYQRQFRKDVIIDLLCYR
QWGHNELDEPFYTNPIMYKIIRARKSIPDTYAEHLIAGGLMTQEEVSEIKSSYYAKLNDHLNNMAHYRPPALNLQAHWQGL
AQPEAQITTWSTGVPLDLLRFVGMKSVEVPRELQMHSHLLKTHVQSRMEKMMDGIKLDWATAEALALGSLLAQGFNVRLS
GQDVGRGTFSQRHAIVVCQETDDTYIPLNHMDPNQKGFLEVSNSPLSEEAVLGFEYGMSIESPKLLPLWEAQFGDFFNGAQI
IFDTFISGGEAKWLLQSGIVILLPHGYDGAGPDHSSCRIERFLQMCDSAEEGVDGDTVNMFVVHPTTPAQYFHLLRRQMVR
NFRKPLIVASPKMLLRLPAAVSTLQEMAPGTTFNPVIGDSSVDPKKVKTLVFCSGKHFYSLVKQRESLGAKKHDFAIIRVEELCP
FPLDSLQQEMSKYKHVKDHIWSQEEPQNMGPWSFVSPRFEKQLACKLRLVGRPPLPVPAVGIGTVHLHQHEDILAKTFASS
KGGYGLNDIFEAQKIEWHE
(underlined sequence contains vector encoded His-tag and TEV protease cleavage site*)

hDLST₆₈₋₄₅₃ for co-infection in Sf9

hDLST$_{68-453}$ for co-infection in Sf9

SGC ID: DLSTA-c017
Vector: pFB-LIC-Bse
Accession: P36957, NM_001933.4
Cell line: Sf9
Tags and additions: His$_6$ tag in 22-aa N-terminal fusion peptide, with TEV protease cleavage site.
Construct Protein Sequence:
MGHHHHHHSSGVDLGTENLYFQ*SMDDLVTVKTPAFAESVTEGDVRWEKAVGDTVAEDEVVCEIETDKTSVQVPSPANG
VIEALLVPDGGKVEGGTPLFTLRKTGAAPAKAKPAEAPAAAAPKAEPTAAAVPPPAAPIPTQMPPVPSPSQPPSGKPVSAVK
PTVAPPLAEPGAGKGLRSEHREKMNRMRQRIAQRLKEAQNTCAMLTTFNEIDMSNIQEMRARHKEAFLKKHNLKLGFMSA
FVKASAFALQEQPVVNAVIDDTTKEVVYRDYIDISVAVATPRGLVVPVIRNVEAMNFADIERTITELGEKARKNELAIEDMDG
GTFTISNGGVFGSLFGTPIINPPQSAILGMHGIFDRPVAIGGKVEVRPMMYVALTYDHRLIDGREAVTFLRKIKAAVEDPRVLL
LDL
(underlined sequence contains vector encoded His-tag and TEV protease cleavage site*)

Site-directed mutations were constructed using the QuikChange mutagenesis kit (Stratagene) and confirmed by sequencing. All primers are available upon request. Wild-type and variant hDHTKD1 proteins were expressed in *E. coli* BL21(DE3)R3-Rosetta cells from 1-6 L of Terrific Broth culture. Cultures were grown at 37°C until an OD of 1.0, when they were cooled to 18°C and induced with 0.1 mM IPTG overnight. Cultures were harvested at 4000 x g for 30 minutes. Cell pellets were lysed by sonication at 35% amplitude, 5 seconds on 10 seconds off, and centrifuged at 35,000 x *g*. The clarified cell extract was incubated with Ni-NTA resin pre-equilibrated with lysis buffer (50 mM HEPES pH 7.5, 500 mM NaCl, 20 mM imidazole, 5% glycerol, 0.5 mM TCEP). The column was washed with 80 ml Binding Buffer (50 mM HEPES pH 7.5, 500 mM NaCl, 5% glycerol, 20 mM imidazole, 0.5 mM TCEP), 80 ml Wash Buffer (50 mM HEPES pH 7.5, 500 mM NaCl, 5% glycerol, 40 mM imidazole, 0.5 mM TCEP) and eluted with 15 ml of Elution Buffer (50 mM HEPES pH 7.5, 500 mM NaCl, 5% glycerol, 250 mM Imidazole, 0.5 mM TCEP). The eluant fractions were concentrated to 5 ml and applied to a Superdex 200 16/60 column pre-equilibrated in GF Buffer (50 mM HEPES pH 7.5, 500 mM NaCl, 0.5 mM TCEP, 5% glycerol). Eluted protein fractions were concentrated to 10-15 mg/ml.

Co-expression of human DHTKD1 and DLST
The hDHTKD1-hDLST complex used in this study was co-expressed in *E. coli* and insect Sf9 cells. For *E. coli* co-expression, hDHTKD1$_{45-919}$ was subcloned into the pCDF-LIC vector (incorporating His-tag) and co-transformed with the plasmid encoding untagged hDLST$_{68-453}$ in the pNIC-CT10HStII vector. Co-transformed cultures were grown and protein purification was performed as described above for hDHTKD1 alone. For co-expression in insect cells, two baculoviruses were produced by transformation of DH10Bac cells, one expressing His-tagged hDHTKD1$_{45-919}$ in pFB-Bio5 vector and one expressing His-tagged hDLST$_{68-453}$ in pFB-LIC-Bse vector. Viruses were amplified by infecting Sf9 insect cells in 250 ml of sf900II serum free, protein-free insect cell medium (Thermo Fisher Scientific) and grown for 65 h at 27°C. Large-scale Sf9 culture was then co-infected in a 1:1 ratio with the two viruses each at 1.5 ml/L. One baculovirus pFB-Bio5 vector expresses His-tagged hDHTKD1$_{45-919}$ and the other baculovirus pFB-LIC-Bse vector expresses His-tagged hDLST$_{68-453}$. The cultures were grown at 27°C for 72 hr in 3L flasks before harvesting at 900 x g for 30 minutes. The purification of Sf9 expressed proteins was performed mostly as above, differing only in the addition of 1:1000 benzonase to the lysis buffer and a gentler sonication cycle of 4 seconds on, 12 seconds off.

Structural biology and biophysical assays
Crystallisation and structure determination of DHTKD1
Crystals were grown by vapour diffusion method. To crystalise hDHTKD1$_{45-919}$, concentrated protein was incubated for 30 minutes on ice with 3 mM MgCl$_2$ and 3 mM ThDP before being centrifuged for 10 minutes at 13500xg to remove any precipitation. Sitting drops containing 75 nL protein (10 mg/mL) and 75 nL well solution containing 20% (w/v) PEG 3350, 0.1 M bis-tris-propane pH 8.5, 0.2 M sodium formate and 10% (v/v) ethylene glycol were equilibrated at 4°C. Crystals were mounted and frozen without additional cryo-protectant, as the crystallisation condition contains 10% (v/v) ethylene glycol. Diffraction data were collected at the Diamond Light Source beamline i04, and processed using the CCP4 program suite (14). hDHTKD1$_{45-919}$ crystallised in the primitive space group *P*1 with two molecules in the asymmetric unit. The structure was solved by molecular replacement using the program *PHASER* (15) and the *E. coli* OGDH structure (PDB code 2JGD) as search model. The structure was refined using *PHENIX* (16), followed by iterative cycles of model building in *COOT* (17)*.

Small angle X-ray scattering
SAXS experiments were performed at 0.99 Å wavelength Diamond Light Source at beamline B21 coupled to the appropriate size exclusion column (Harwell, UK) and equipped with Pilatus 2M two-dimensional detector at 4.014 m distance from the sample, $0.005 < q < 0.4$ Å^{-1} ($q = 4\pi \sin \theta/\lambda$, 2θ is the scattering angle). hDHTKD1$_{45-919}$ at 20 mg/ml in 10 mM Hepes-NaOH pH 7.5, 200 mM NaCl, 0.5 mM TCEP and 2% glycerol was applied onto the Shodex KW404-4F column.

SAXS measurements were performed at 20°C, using an exposure time of 3 seconds per frame. SAXS data were processed and analyzed using the ATSAS program package (20) and Scatter (http://www.bioisis.net/scatter). The radius of gyration Rg and forward scattering I(0) were calculated by Guinier approximation. The maximum particle dimension Dmax and P(r) function were evaluated using the program GNOM (21).

Solution analysis

Analytical gel filtration was performed on a Superdex 200 Increase 10/300 GL column or Superose 6 Increase 10/300 GL (GE Healthcare) pre-equilibrated with 20 mM HEPES pH 7.5, 150 mM NaCl and 0.5 mM TCEP.

Differential scanning fluorimetry (DSF)

DSF was performed in a 96-well plate using an Mx3005p RT-PCR machine (Stratagene) with excitation and emission filters of 492 and 610 nm, respectively. Each well (20 µl) consisted of protein (2 mg/ml in 100 mM Hepes pH 7.5, 150 mM NaCl, 5% glycerol), SYPRO-Orange (Invitrogen, diluted 1000-fold of the manufacturer's stock). Fluorescence intensities were measured from 25 to 96 °C with a ramp rate of 1 °C/min. T_m was determined by plotting the intensity as a function of temperature and fitting the curve to a Boltzmann equation. Temperature shifts, ΔT_m, were determined as described (22) and final graphs were generated using GraphPad Prism (v.7; Graph-Pad Software). Assays were carried out in technical triplicate

MIDAS protein-metabolite screening

Protein-metabolite interaction screening using an updated MIDAS platform was performed similar to (11). Briefly, a flow injection analysis-mass spectrometry (FIA-MS) validated library of 412 metabolite standards were combined into four defined screening pools in 150 mM ammonium acetate pH 7.4. For each metabolite pool, 5 µl of target protein was arrayed in triplicate across a SWISSCI 10 MWC 96-well microdialysis plate (protein chambers). To the trans side of each dialysis well, 300 µl of a 50 µM metabolite pool supplemented with 1 mM ThDP and 1 mM $MgCl_2$ were arrayed in triplicate per hDHTKD1$_{45-919}$ protein (metabolite chambers). Dialysis plates were placed in the dark at 4°C on a rotating shaker (120 rpm) and incubated for 40 hours. Post-dialysis, protein and metabolite chamber dialysates were retrieved, normalised and diluted 1:10 in 80% methanol, incubated 30 min on ice, and centrifuged at 3200 rcf for 15 min to remove precipitated protein. Analytes were aliquoted across a 384-well microvolume plate and placed at 4°C in a Shimadzu SIL-20ACXR autosampler for FIA-MS analysis. 2 µl of each sample was analysed in technical triplicate by FIA-MS on a SCIEX X500R QTOF MS with interspersed injections of blanks.

MIDAS data analysis

FIA-MS spectra collected from MIDAS protein-metabolite screening was qualitatively and quantitatively processed in SCIEX OS 1.5 software to determine relative metabolite abundance by integrating the mean area under the curve (AUC) across technical triplicates. Log2(fold change) for each metabolite was calculated from the relative metabolite abundance in the protein chamber (numerator) and metabolite chamber (denominator) from dialysis triplicates. For each technical triplicate, up to one outlier was removed using a z-score cut-off of five (< 0.1% of observations). The corrected technical replicates were collapsed to one mean fold-change summary per protein-metabolite pair. To remove fold-change variation that was not specific to a given metabolite-protein pair, the first three principal components of the cumulative screening dataset were removed (~75% of observed variance) creating Log2(corrected fold change). Protein-metabolite z-scores were determined by comparing the target protein-metabolite Log2(corrected fold change) to a no-signal model for that metabolite using measures of the central tendency (median) and standard deviation (sd extrapolated from the 25%-75% quantiles) which are not biased by the signals in the tails of a metabolite's fold-change distribution. Z-scores were false-discovery rate controlled using Storey's q-value (http://github.com/jdstorey/qvalue). Protein-metabolite interactions with p-values < 0.05 and q-values < 0.1 were considered significant.

Grid preparation and EM data collection

3 µl of 0.4 mg/ml purified hDHTKD1$_{45-919}$-hDLST$_{68-453}$ sample from Sf9 cells expression were applied to the glow-discharged Quantifoil Au R1.2/1.3 grid (Structure Probe). Blotting and vitrification in liquid ethane was carried out using a Vitrobot Mark IV (FEI Company) at 4 °C, 95% humidity with a nine second wait and a three second blot at zero blotting force from both sides. Cryo grids were loaded into a Glacios transmission electron microscope (ThermoFisher Scientific) operating at 200 keV with a Falcon3 camera. Movies were recorded in linear mode with a pixel size of 0.96 Å, a defocus range of -1 to -3.1 µm (steps of 0.3 µm), a total dose of 32.52 e/A^2 with 1s exposure over 19 frames.

EM data processing

A total of 619 dose-fractioned movies were corrected for drift using Relion's MotionCor2 (23) with the dose-weighting option. Contrast transfer function (CTF) parameters were determined by ctffind4.1 (24). A subset of 1,244 particles were manually picked and extracted with a box size of 344 pixels rescaled to 172 pixels. 8 classes were selected from one round of 2D classification for reference based auto picking using Relion 3.0 (25). 165,739 particles were extracted with a box size of 344 pixels rescaled to 172 pixels. All downstream particle classification, refinement and post-processing steps were performed in Relion 3.0. The resulting 3,356 particles were refined to a global resolution of 4.7 Å based on the FSC 0.143 threshold criterion.

EM Model building and refinement

Model building and refinement was carried out using the suite of programmes in CCP-EM (26). To fit a template to the final map the *E. coli* DLST orthologue structure (PDB 1SCZ) was used. The sequence was humanised and residues truncated to the alpha carbon using Chainsaw (27). The oligomeric structure was docked into the density map, sharpened with a B-factor of -281 Å^2, using Molrep. One round of refinement using refmac5 was carried out with ProSMART restraints generated from the *E. coli* DLST orthologue to avoid overfitting. Overfitting was monitored through simultaneous refinement against the two half maps from the final 3D refinement. FSC between map and model was calculated using model validation in CCP-EM.

Crystallography-based fragment screening

To grow crystals for fragment screening campaign, hDHTKD1$_{45-919}$ at 10mg/mL was incubated for 30 minutes on ice with 3mM MgCl$_2$ and 3mM ThDP before being centrifuged for 10 minutes at 13500xg to remove any precipitation. Crystals were grown by vapour diffusion in 400 nL sitting drops in the presence of seeds, at 20°C equilibrated against well solutions of 0.1M MgCl2, 0.1M Hepes pH 7.0, 20% PEG 6K, 10% ethylene glycol.

For soaking, 50 nL of each fragment compound from the XChem fragment library (final concentration of 50 mM) was added to a crystallisation drop using an ECHO acoustic liquid handler dispenser at the Diamond Light Source XChem facility. Crystals were soaked for two hours with fragments from the Diamond-SGC Poised Library before being harvested using XChem SHIFTER technology, cryo-cooled in liquid nitrogen and data sets collected at the beamline I04-1 in "automated unattended" mode. The XChem Explorer pipeline (28) was used for structure solution with parallel molecular replacement using DIMPLE (29), followed by map averaging and statistical modelling to identify weak electron densities generated from low occupancy fragments using PANDDA software (30). Coordinates and structure factors for exemplary data sets with bound fragments are deposited in the RCSB Protein Data Bank.

Assays

DHTKD1 enzyme assay

The enzymatic activity assay was performed in triplicates, in a buffer containing 35 mM potassium phosphate (KH$_2$PO$_4$), 0.5 mM EDTA, 0.5 mM MgSO$_4$, 2 mM 2OA or 2OG, 1 mM ThDP, 5 mM sodium azide (NaN$_3$) and 60 µM 2,6-dichlorphenol indophenol (DCPIP), pH 7.4. The activity was determined as a reduction of DCPIP at λ= 610-750 nm, 30°C (18) with and without 2OA or 2OG. The dye DCPIP changes colour from blue to colourless, when being reduced (19). To obtain K_m and V_{max} different concentrations of 2OA (0.1 mM, 0.05 mM, 0.1 mM, 0.25 mM, 0.5 mM, 0.75 mM, 1 mM, 2 mM) and no substrate were measured in a 96-well micro titre plate (total well volume 300 µl). The ensuing OD values were plotted on a graph (slope= 1/V_{max}; Y-intercept= K_m/V_{max}) to calculate K_m and V_{max} using the Hanes Woolf plot:

$$\frac{[S]}{V0} = \frac{[s]}{Vmax} + \frac{Km}{Vmax}$$

V_0= initial velocity; [S]= substrate concentration; V_{max}= maximum velocity.

References

1. Perham, R. N. (1991) Domains, motifs, and linkers in 2-oxo acid dehydrogenase multienzyme complexes: a paradigm in the design of a multifunctional protein. *Biochemistry*. **30**, 8501–8512

2. Marrott, N. L., Marshall, J. J., Svergun, D. I., Crennell, S. J., Hough, D. W., van den Elsen, J. M., and Danson, M. J. (2014) Why are the 2-oxoacid dehydrogenase complexes so large? Generation of an active trimeric complex. *Biochem J*. **463**, 405–412

3. Zhang, X., Nemeria, N. S., Leandro, J., Houten, S., Lazarus, M., Gerfen, G., Ozohanics, O., Ambrus, A., Nagy, B., Brukh, R., and Jordan, F. (2020) Structure-function analyses of the G729R 2-oxoadipate dehydrogenase genetic variant associated with L-lysine metabolism disorder. *J. Biol. Chem.* **295**, 8078–8095

4. Hedlund, G. L., Longo, N., and Pasquali, M. (2006) Glutaric acidemia type 1. *Am. J. Med. Genet. - Semin. Med. Genet.* **142 C**, 86–94

5. Danhauser, K., Sauer, S. W., Haack, T. B., Wieland, T., Staufner, C., Graf, E., Zschocke, J., Strom, T. M., Traub, T., Okun, J. G., Meitinger, T., Hoffmann, G. F., Prokisch, H., and Kölker, S. (2012) DHTKD1 mutations cause 2-aminoadipic and 2-oxoadipic aciduria. *Am. J. Hum. Genet.* **91**, 1082–1087

6. Yue, W. W., Mackinnon, S., and Bezerra, G. A. (2019) Substrate reduction therapy for inborn errors of metabolism. *Emerg. Top. Life Sci.* **3**, 63–73

7. Bezerra, G. A., MacKinnon, S., McCorvie, T., Zhang, M., Tang, M., Foster, W., Fairhead, M., Tumber, A., Strain-Damerell, C., Kopec, J., Fitzpatrick, F., Whitby, F., Hill, C. P., Lai, K., and Yue, W. W. (2019) Human Galatose-1-phosphate Uridylyltransferase (GALT), Galactokinase 1 (GALK1); A Target Enabling Package. doi.org/10.5281/ZENODO.3250158

8. Kopec, J., Pena, I., Rembeza, E., Mclaughlin, M., Strain-damerell, C., Goubin, S., Mackinnon, S., Burgess-brown, N., Brennan, P., Mackenzie, A., Arruda, P., Yue, W. W., Goubin, S., Mackinnon, S., Burgess-, N., Brennan, P., Mackenzie, A., Arruda, P., and Yue, W. (2017) *Human Alpha-Aminoadipic Semialdehyde Synthase,* doi.org/10.5281/zenodo.1219674

9. MacKinnon, S., Bezerra, G. A., Krojer, T., Bradley, A. R., Talon, R., Brandao-neto, J., Douangamath, A., Oppermann, U., von Delft, F., Brennan, P. E., and Yue, W. W. (2018) *Human Hydroxyacid,* doi.org/10.5281/zenodo.1344541

10. Bezerra, G. A., Bailey, H. J., Marcero, J. R., Foster, W. R., Rembeza, E., Dailey, H. A., and Yue, W. W. (2019) *Human 5'-Aminolevulinate Synthase, Erythroid-Specific (ALAS2),* doi.org/10.5281/zenodo.4153550

11. Orsak, T., Smith, T. L., Eckert, D., Lindsley, J. E., Borges, C. R., and Rutter, J. (2012) Revealing the allosterome: systematic identification of metabolite-protein interactions. *Biochemistry*. **51**, 225–232

12. Knapp, J. E., Mitchell, D. T., Yazdi, M. A., Ernst, S. R., Reed, L. J., and Hackert, M. L. (1998) Crystal structure of the truncated cubic core component of the Escherichia coli 2-oxoglutarate dehydrogenase multienzyme complex. *J Mol Biol*. **280**, 655–668

13. Parthasarathy, A., Pierik, A. J., Kahnt, J., Zelder, O., and Buckel, W. (2011) Substrate specificity of 2-hydroxyglutaryl-CoA dehydratase from clostridium symbiosum: Toward a bio-based production of adipic acid. *Biochemistry*. **50**, 3540–3550

14. CCP4 (1994) The CCP4 suite: programs for protein crystallography. *Acta Crystallogr. D Biol. Crystallogr.* **50**, 760–763

15. McCoy, A. J., Grosse-Kunstleve, R. W., Storoni, L. C., and Read, R. J. (2005) Likelihood-enhanced fast translation functions. *Acta Crystallogr. D Biol. Crystallogr.* **61**, 458–464

16. Adams, P. D., Afonine, P. V, Bunkoczi, G., Chen, V. B., Davis, I. W., Echols, N., Headd, J. J., Hung, L. W., Kapral, G. J., Grosse-Kunstleve, R. W., McCoy, A. J., Moriarty, N. W., Oeffner, R., Read, R. J., Richardson, D. C., Richardson, J. S., Terwilliger, T. C., and Zwart, P. H. (2010) PHENIX: a comprehensive Python-based system for macromolecular structure solution. *Acta Crystallogr D Biol Crystallogr*. **66**, 213–221

17. Emsley, P., and Cowtan, K. (2004) Coot: model-building tools for molecular graphics. *Acta Crystallogr. D Biol. Crystallogr.* **60**, 2126–2132

18. Sauer, S. W., Okun, J. G., Schwab, M. A., Crnic, L. R., Hoffmann, G. F., Goodman, S. I., Koeller, D. M., and Kolker, S. (2005) Bioenergetics in glutaryl-coenzyme A dehydrogenase deficiency: a role for glutaryl-coenzyme A. *J Biol Chem*. **280**, 21830–21836

19. VanderJagt, D. J., Garry, P. J., and Hunt, W. C. (1986) Ascorbate in plasma as measured by liquid chromatography and by dichlorophenolindophenol colorimetry. *Clin Chem*. **32**, 1004–1006

20. Petoukhov, M. V, Franke, D., Shkumatov, A. V, Tria, G., Kikhney, A. G., Gajda, M., Gorba, C., Mertens, H. D., Konarev, P. V, and Svergun, D. I. (2012) New developments in the ATSAS program package for small-angle scattering data analysis. *J Appl Crystallogr*. **45**, 342–350

21. Svergun, D. I. (1992) Determination of the regularization parameter in indirect-transform methods using perceptual criteria. *J App Cryst*. **25**, 495–503

22. Niesen, F. H., Berglund, H., and Vedadi, M. (2007) The use of differential scanning fluorimetry to detect ligand interactions that promote protein stability. *Nat Protoc*. **2**, 2212–2221

23. Zheng, S. Q., Palovcak, E., Armache, J. P., Verba, K. A., Cheng, Y., and Agard, D. A. (2017) MotionCor2: anisotropic correction of beam-induced motion for improved cryo-electron microscopy. *Nat Methods*. **14**, 331–332

24. Rohou, A., and Grigorieff, N. (2015) CTFFIND4: Fast and accurate defocus estimation from electron micrographs. *J Struct Biol*. **192**, 216–221

25. Scheres, S. H., and Chen, S. (2012) Prevention of overfitting in cryo-EM structure determination. *Nat Methods*. **9**, 853–854

26. Burnley, T., Palmer, C. M., and Winn, M. (2017) Recent developments in the CCP-EM software suite. *Acta Crystallogr D Struct Biol*. **73**, 469–477

27. Stein, N. (2008) CHAINSAW: a program for mutating pdb files used as templates in molecular replacement. *J. Appl. Crystallogr.* **41**, 641–643

28. Krojer, T., Talon, R., Pearce, N., Collins, P., Douangamath, A., Brandao-Neto, J., Dias, A., Marsden, B., and Von Delft, F. (2017) The XChemExplorer graphical workflow tool for routine or large-scale protein-ligand structure determination. *Acta Crystallogr. Sect. D Struct. Biol.* **73**, 267–278

29. Winn, M. D., Ballard, C. C., Cowtan, K. D., Dodson, E. J., Emsley, P., Evans, P. R., Keegan, R. M., Krissinel, E. B., Leslie, A. G. W., McCoy, A., McNicholas, S. J., Murshudov, G. N., Pannu, N. S., Potterton, E. A., Powell, H. R., Read, R. J., Vagin, A., and Wilson, K. S. (2011) Overview of the CCP4 suite and current developments. *Acta Crystallogr. Sect. D Biol. Crystallogr.* **67**, 235–242

30. Pearce, N. M., Krojer, T., Bradley, A. R., Collins, P., Nowak, R. P., Talon, R., Marsden, B. D., Kelm, S., Shi, J., Deane, C. M., and Von Delft, F. (2017) A multi-crystal method for extracting obscured crystallographic states from conventionally uninterpretable electron density. *Nat. Commun.* **8**, 24–29

We respectfully request that this document is cited using the DOI value as given above if the content is used in your work.